Elsevier Editorial System(tm) for Journal of Atmospheric and Solar-Terrestrial Physics
Manuscript Draft

Manuscript Number:

Title: Phase Functions of Polar Mesospheric Cloud Ice as Observed by the CIPS Instrument on the AIM Satellite

Article Type: Special Issue:Summer Mesopause-LPMR

Keywords: Polar Mesospheric Clouds; Noctilucent Clouds; PMC; AIM; Mesosphere; Clouds

Corresponding Author: Dr. Scott Martin Bailey, PhD

Corresponding Author's Institution: Virginia Tech

First Author: Scott Martin Bailey, PhD

Order of Authors: Scott Martin Bailey, PhD; Gary E Thomas, PhD; David W Rusch, PhD; Aimee W Merkell, PhD; Christian D Jeppesen; Justin N Carstens; Cora E Randall, PhD; William E McClintock, PhD; James M Russell, PhD

Abstract: The Cloud Imaging and Particle Size (CIPS) instrument on the AIM spacecraft is a 4-camera nadir pointed imager with a bandpass centered at 265 nm and a field of view of 120 by 80 degrees. CIPS observes Polar Mesospheric Clouds (PMCs) against the sunlit Rayleigh-scattered background. At individual polar locations approximately 5 by 5km in area, CIPS observes the same volume of air seven times over a range of scattering angles from about 35 to 150 degrees. These multi-angle observations allow the identification and extraction of the PMC scattered radiance from the Rayleigh-scattered background. We utilize the fact that the former has a highly asymmetric phase function about 90° scattering angle, while the latter has a phase function that is symmetric. The retrieved PMC phase function can then be interpreted to obtain PMC particle size distributions. We describe a technique for identification of PMCs in the CIPS observations through the separation of the Rayleigh and PMC radiances. PMC phase function results are shown for the first season of CIPS observations. Assuming the particles are oblate spheroids with an axial ratio of 2, and a Gaussian distribution of width 14 nm, we find the phase functions are consistent with mean radii between 50 and 60 nm. These results are similar to those discussed by Hervig et al. [2008] in this issue from the Solar Occultation for Ice Experiment (SOFIE) which also flies on the AIM satellite.

Manuscript
Click here to download Manuscript: Bailey et al CIPS Phase Functions 2008 Submitted No Figures.doc Click here to view linked References

Phase Functions of Polar Mesospheric Cloud Ice as Observed by the CIPS Instrument on the AIM Satellite

Scott M. Bailey[1], Gary E. Thomas[2], David W. Rusch[2], Aimee W. Merkel[2], Christian D. Jeppesen[2], Justin N. Carstens[1], Cora E. Randall[2], William E. McClintock[2], James M. Russell, III[3]

[1]Bradley Department of Electrical and Computer Engineering, Virginia Tech, Blacksburg, VA 24061

[2]Laboratory for Atmospheric and Space Physics, University of Colorado, Boulder, CO 80303

[3]Center for Atmospheric Sciences, Hampton University, Hampton, VA 23668

Abstract

The Cloud Imaging and Particle Size (CIPS) instrument on the AIM spacecraft is a 4-camera nadir pointed imager with a bandpass centered at 265 nm and a field of view of 120 by 80 degrees. CIPS observes Polar Mesospheric Clouds (PMCs) against the sunlit Rayleigh-scattered background. At individual polar locations approximately 5 by 5km in area, CIPS observes the same volume of air seven times over a range of scattering angles from about 35 to 150 degrees. These multi-angle observations allow the identification and extraction of the PMC scattered radiance from the Rayleigh-scattered background. We utilize the fact that the former has a highly asymmetric phase function about 90° scattering angle, while the latter has a phase function that is symmetric. The retrieved PMC phase function can then be interpreted to obtain PMC particle size distributions. We describe a technique for identification of PMCs in the CIPS observations through the separation of the Rayleigh and PMC radiances. PMC phase function results are shown for the first season of CIPS observations. Assuming the particles are oblate spheroids with an axial ratio of 2, and a Gaussian distribution of width 14 nm, we find the phase functions are

consistent with mean radii between 50 and 60 nm. These results are similar to those discussed by Hervig et al. [2008] in this issue from the Solar Occultation for Ice Experiment (SOFIE) which also flies on the AIM satellite.

1.0 Introduction

Polar Mesospheric Clouds (PMCs) are a high-latitude, summertime phenomenon that has generated significant interest in recent decades. PMCs were first observed in 1885 [Leslie, 1885] and there is evidence that their brightness and frequency of occurrence have been increasing since at least 1979 [Shettle et al., 2002; DeLand et al., 2003; 2007]. Hemispheric differences in their spatial and temporal morphology have been found [see Bailey et al., 2007 and references there in]. Evidence for control of their morphology by solar forcing [DeLand et al., 2007], geomagnetic forcings [von Savigny et al., 2007], lower atmosphere meteorology [Berger and Leubken, 2006], and winter hemisphere stratospheric dynamics [Karlsson et al., 2007] have also been shown. It has been suggested (and debated) that increases in their occurrence frequency and brightness are linked to global change [Thomas 2003, see also von Zahn, 2003 and Thomas et al., 2003]. A complete understanding of the variability of PMCs and any potential link to climate change is hindered by an incomplete understanding of the microphysics of these clouds [Rapp and Thomas, 2006].

The scattering phase function of PMC ice is an important quantity for understanding PMC microphysics. The phase functions are directly related to the size distribution, index of refraction, and shape of the ice particles [Rapp et al., 2007]. Although only a limited number of space based-observations of PMC scattering phase functions exist [Gumbel et al., 2001], bidirectional observations of PMCs by the Student Nitric Oxide Explorer [SNOE, Bailey et al., 2005] and the Solar Mesosphere Explorer [SME, Thomas, 1984] have inferred some information about the PMC phase function and utilized it to infer particle sizes [Thomas and McKay, 1985; Rusch et al., 2008]. In this work we describe the first satellite observations of PMC ice phase functions.

51 The Cloud Imaging and Particle Size (CIPS) instrument on the Aeronomy of the Ice in the
52 Mesosphere (AIM) satellite was designed to image PMCs from space and to determine their ice
53 scattering phase function at high spatial resolution (~5 km) over the summer polar cap. This is
54 accomplished by observing PMCs below the spacecraft at multiple angles and determining the
55 angular dependence of the cloud brightness against the background Rayleigh scattered sunlight
56 background. AIM was launched on April 25, 2007 and routine observations by CIPS began on
57 May 24, 2007. At this time, AIM has observed one full Northern (2007) and most of the Southern
58 (2007 / 2008) PMC season. Since the purpose of this paper is primarily to describe a technique
59 for obtaining phase functions, we will focus on only a few orbits. In a future work we will
60 describe the morphology of PMC phase functions and compare the obtained phase functions in
61 the northern and southern hemispheres. For now, we describe the algorithm for isolating the
62 PMC brightness from the Rayleigh background and for obtaining the phase functions.

63 **2.0 Observations**

64 The goals of the CIPS instrument are described in this issue by Rusch et al. [2008]. The details of
65 the instrument design and its implantation on AIM are also described in this issue by McClintock
66 et al. [2008]. See also Russell et al. [2008] for the objective of the AIM mission and the other
67 instruments. Here only a brief description and list of the relevant CIPS details are presented.
68 CIPS consists of an array of four cameras operating with a 15 nm passband centered at 265 nm.
69 Each camera has an overlapping FOV and a spatial resolution (at the nadir) of 1 x 2 km. The
70 FOV of the camera system is 80º x 120º, centered at the sub-satellite point, with the 120º axis
71 along the orbit track. Because of slant viewing, the spatial resolution increases to 6.4 km near
72 the edge of the FOV of the forward and aft cameras. The combination of images from the four
73 cameras is referred to as a scene. CIPS records scenes of atmospheric and cloud radiance in the
74 summer hemisphere from the terminator to ~40° latitude over the sunlit portion of the orbit.

75 Each camera has a focal ratio of 1.12, a focal length of 28 mm, and a 25 mm lens diameter and

76 includes an interference filter and a Charge Coupled Device (CCD) detector system. The
77 throughput of the optical elements and their sizes are designed for a ±1% measurement precision
78 of the background sunlit Earth. The CCD detectors are coupled with image intensifiers and have
79 2048 x 2048 useful pixels that are electronically binned in 4 x 8 combinations for an effective
80 340 (cross track) x 170 (along track) pixel images. The instantaneous field-of-view of an
81 effective picture element is 1 x 2 km projected at the cloud height of 83 km. On average, 26
82 images are produced per orbit in the summer polar region with special 'first light' images just
83 beyond the terminator.

84 Imaging is achieved with this body-fixed camera assembly using an exposure time of 1 second.
85 Scenes are obtained at a cadence of one per 43 seconds. This fact combined with the large field
86 encompassed by a scene results in between four and seven exposures of the same spatial element
87 for each satellite overpass. Each of these observations of the same spatial elements is made at a
88 different scattering and observation angle. The scattering angle, Θ, is the angle between the
89 unscattered photon path and the new path after the scattering. The observation angle, ϕ, is the
90 angle between the zenith and the CIPS line of site (from the ice perspective). In this paper, we
91 refer to the variation of the observed albedo as a function of scattering angle (or observation
92 angle) as a scattering profile. Note that all symbols used in this paper are defined in the
93 Appendix.

94 The range of scattering angles over which an individual location is observed varies along the
95 orbit. At high solar zenith angles, close to the terminator, a nadir observation is near $\Theta = 90°$.
96 Thus observations sunward of nadir yield forward scattered observations ($\Theta < 90°$ and
97 observations anti-sunward produce backward scattered observations ($\Theta > 90°$). As the satellite
98 moves along the orbit to the subsolar point, nadir observations are at $\Theta = 180°$ and observations
99 on either side of nadir are such that $90° < \Theta < 180°$. No forward scattered observations can be
100 made by CIPS at the subsolar point.

Figure 1 shows the range of scattering angles per scattering profile as a function of solar zenith angle. The points on this Figure are from Orbit 424 on May 24 but would be similar for any day of CIPS operation. An observation is identified by a single grey point on this figure (every 4th observation is plotted). For select locations, the scattering profile is shown using asterisk connected by solid lines. At high solar zenith angles, approximately half of the observations are at $\Theta < 90°$ and half are at $\Theta > 90°$. At progressively lower solar zenith angles, a larger fraction of the observations are made at $\Theta > 90°$.

3.0 Sources of Observed Radiance

The radiance observed by CIPS is due to two sources. The first is scattered solar radiance due to ice crystals in PMCs. PMCs are present throughout the summer polar region. The second, ever present, source is singly-scattered solar radiance due to Rayleigh scattering by atmospheric molecules. Even for the brightest PMCs, Rayleigh scattering is the dominant source of radiance. In this section we describe analytic representations of both sources. These analytic expressions will serve as the basis for the retrievals discussed in the following section.

Throughout this work and in general for all CIPS products, radiances are expressed in albedo, the ratio of atmospheric radiance to solar irradiance. The calculation of albedo from CIPS observations is discussed in both Rusch et al. [2008] and McClintock et al. [2008]. The units of albedo are sr^{-1}. We use the symbol G to refer to albedo units of 10^{-6} sr^{-1}.

We write the observed albedo due to PMC ice, A_{ice}, as

$$A_{ice} = \frac{A_{PMC} P_{ice}}{\cos(\phi)} \qquad (1)$$

We define the albedo of a PMC, A_{PMC}, as the albedo which would be observed at $\Theta = 90°$. A_{PMC} contains information about the ice column density, particle size and shape, and index of refraction. P_{ice} is the ice scattering phase function. With the definitions used here, this phase

function is normalized to unity at $\Theta = 90°$. The $\cos(\phi)$ factor corrects for slant path geometry when viewing the cloud off nadir.

The non-cloud brightness is due to Rayleigh scattering of sun light from N_2 and O_2 molecules. At 265 nm, the observed brightness is due to a single scattering and is strongly controlled by ozone absorption along the path. This wavelength was chosen for CIPS because it is near this wavelength that ozone absorption peaks and thus provides the greatest contrast between atmospheric and PMC brightness. Calculations of the limb brightness for similar wavelengths are discussed by Merkel at al. [2001] for limb geometries and McPeters [1980] for nadir geometries. At most solar zenith angles, the peak contribution to the observed nadir viewing 265 nm Rayleigh brightness is from 50 to 55 km. Near 90° solar zenith angle, this altitude rapidly increases to 65 km.

In order to describe the atmospheric albedo due to Rayleigh scattering analytically, we generalize the result of McPeters [1980]. They provided an analytic result for single scattering, neglecting attenuation along the path by Raleigh scattering, and assuming that the ratio of the ozone scale height to the atmospheric scale height, σ, was constant. We generalize their result to allow for off-nadir viewing as

$$A_{Ray} = \frac{P_{Ray}(\Theta)\Gamma(\sigma+1)\beta N(z_0)}{\mu_V\left(\frac{1}{\mu_V}+\frac{1}{\mu_Z}\right)^{\sigma}\alpha^{\sigma}C(z_0)^{\sigma}} \qquad (2)$$

where $P_{Ray}(\Theta)$ is the known Rayleigh phase function, Γ is the Gamma function, β is the cross section for Rayleigh scattering, α is the cross section for pure absorption by ozone, N is the column density of atmospheric molecules above a reference altitude, z_0, and C is the column density of ozone molecules above that reference altitude. A full derivation of Equation 2 is provided in the appendix. The factors μ_V and μ_Z are path-length factors that account for the slant

path through atmospheric layers. For vertical paths their value is unity. As CIPS views off nadir such that the ϕ increases from zero, μ_V varies as cos(ϕ). Similarly as the solar zenith angle, θ, increases, the path-length factor initially varies as cos(θ). For θ larger than 80°, a cosine approximation is inadequate and a Chapman function correction [Chapman, 1931] must be applied. See Fitzmaurice [1964] for an implementation of the Chapman function. We specify the solar zenith angle for each scattering profile as that solar zenith angle appropriate to the altitude of peak Rayleigh contribution, typically near 55 km.

Although the reference altitude, z_0, appears in Equation 2, the equation does not depend directly on altitude. The column densities must however be consistently referenced to a particular altitude which we label z_0. In our applications, we specify an air column density, N, of 2.4 x 10^{22} cm^{-2} which occurs near 50 km [Hedin et al., 1986]. This means that any ozone column density obtained from CIPS observations and the algorithms presented here (unless otherwise corrected) is the number of molecules in a vertical column above the altitude at which the vertical column density of air molecules is 2.4 x 10^{22} cm^{-2}. We adopt an ozone absorption cross section at 265 nm of 9.261x10^{-18} cm^2 and a Rayleigh scattering cross section of 9.708x10^{-26} cm^2[Bates, 1984].

4.0 Cloud-Free Radiance

Equation 2 possesses very useful properties. We arrange Equation 2 to place the geometry factors on one side and the geometry dependant factors on the other. Defining Y and X as

$$Y = \log\left(\frac{1}{\mu_V} + \frac{1}{\mu_Z}\right) \quad (3)$$

and

$$X = \log\left(\frac{A_{Ray}\mu_V}{P_{Ray}(\Theta)}\right). \quad (4)$$

It is easily shown that

168 $$Y = -\sigma X + \text{ constant.} \quad (5)$$

169 Thus from an observed scattering profile, the slope of the line formed by Y versus X yields the
170 negative of σ. With σ obtained, one can use Equation 2 to solve for C. We refer to this as an
171 "analytic retrieval" for C and σ. It is a rapid and powerful method for analyzing a scattering
172 profile that is thought not to contain radiance from PMCs.

173 We demonstrate the validity of Equations 2 through 5 by examining observations on a CIPS orbit
174 that shows no evidence of PMCs. Orbit 424 from May 24, 2007 is such an orbit. There is no
175 structure or behavior in the CIPS images for that day that suggests the presence of any PMC
176 radiance. We use this orbit then as a baseline cloud-free orbit. Figure 2 shows scattering profiles
177 and Y versus X plots for typical observations near 60°, 70°, 80°, and 90° solar zenith angle. In all
178 cases Y shows a good linear relationship with X. The values of C and σ that are obtained from
179 the intercept and slope of this line are used in Equation 2 to provide a model scattering profile
180 that is compared with the observations. The agreement is excellent. For solar zenith angles ≤ 90°
181 we have found that model scattering profiles calculated from inferred C and σ reproduce
182 observed cloud-free scattering profiles to within 2% (and typically less than 1%) for any viewing
183 or scattering angle. This value is at about the level of the random noise of the CIPS observations
184 and so we conclude that Equations 2 through 5 describe the cloud-free observations very well
185 and are adequate for use in CIPS data analysis as descriptions of the Rayleigh component to an
186 observed CIPS scattering profile.

187 An indicator of cloud presence may be defined by looking for deviations from the linear
188 relationship of Equation 5. Because ice radiance is heavily forward scattered [Bailey et al., 2007;
189 Rusch et al., 2008], the departure from Equation 5 will be most evident at small scattering
190 angles. There are many possible definitions for a cloud indicator that take advantage of this fact.
191 We have found the following to provide the best results. For each scattering profile, we calculate
192 a slope for Y versus X from observations with scattering angles less than 90° and also from

observations with scattering angles greater than 90°. We then divide each group of observations by the appropriate linear fit. For perfect observations all of the resulting values would be unity. We take the mean of the forward scattered results and divide by the mean of the backward scattered results. For cloud-free observations, this value should be very near unity. Where clouds are present, the forward scattered values will be most affected and the resulting ratio will be less than one. We refer to this ratio as RATALL.

Figure 3 shows the distribution of values of RATALL for all scattering profiles in Orbit 424 between solar zenith angles of 60° and 90°. The distribution is symmetric about unity with a standard deviation of 0.015. This distribution is exactly as would be expected for cloud free observations with random noise corresponding to the CIPS sensitivity. Figure 3 also shows the same distributions for two other orbits, 684 on June 10, 2007 and 1113 on July 9, 2007, where clouds are expected to be present. These orbits were selected because Orbit 684 is representative of an orbit containing many patches of clouds of average (according to CIPS) brightness while Orbit 1113 is one of the orbits with the most and brightest clouds that have been observed by CIPS. The presence of PMCs are easily seen in this distribution by the populations of RATALL values lower than 1.0 and outside the lower side of the orbit 424 distribution. Two standard deviations below the mean of 1.0 for Orbit 424 is the value 0.995. We assume any scattering profile with a RATALL value less than 0.995 should be flagged as likely to contain a PMC signature.

5.0 Retrieval Method

The most crucial step in obtaining PMC properties from CIPS data is separating the ice and Rayleigh scattering contributions. In this section we describe a process for performing that separation. From the above discussion, we have a general description for all CIPS observed scattering profiles

$$A_{CIPS} = A_{Ray} + A_{ice} . \quad (6)$$

There are four unknowns in Equation 6: C, σ, A_{PMC}, and P_{ice}. The ice phase function, P_{ice}, is dependent upon the mean particle size and shape, the shape of the distribution of particles sizes, and the width of that distribution. In order to minimize the number of unknowns in our analysis, we assume the particles are oblate spheroids with an axial ratio of 2 [Eremenko et al., 2005; Hervig et al., 2008] and have a Gaussian distribution with a width of 14 nm [Rapp and Thomas, 2006]. This reduces the description of P_{ice} to a single free parameter, the mean particle size or mode radius, R_m. We then use numerical representations of P_{ice} for these assumptions and R from 0 to 300 nm created from the T-matrix model of Mishchenko and Travis [1998]. We emphasize that the stated assumptions are used only to separate the Rayleigh and ice components of the observed radiance and to obtain the ice phase function. Any subsequent interpretation of the retrieved phase function does not require these assumptions. This point will be clarified later.

For all locations that meet the RATALL < 0.995 criteria and when CIPS obtains at least 7 observations including at least two points with scattering angles less than 90°, the following process is performed. A non-linear least-squares fit is performed to solve Equation 6 for the unknowns C, σ, A_{PMC}, and R_m. While 7 unique observations are nominally sufficient to determine 4 unknowns, we have found that providing constraints on C and σ greatly improves the results. There are numerous methods for obtaining suitable constraints. For example one could find the distributions of C and σ from cloud free observations (RATALL > 0.995) using the analytic retrieval and constrain the retrieved C and σ to be within 2 standard deviations of the mean cloud-free C and σ. We have found however that approximate values for C and σ can be obtained from each scattering profile directly even in the presence of a PMC. Because the ice scattering phase functions are so strongly peaked, PMCs generally contribute very little radiance for scattering angles ≥120°. Through simulations, we have found that performing an analytic retrieval on scattering profiles including only observations at scattering angles greater than 120° yields C and σ results that are never different from the true C and σ by more than 12% (3

standard deviations) even for bright clouds. This result changes only negligibly depending on the assumption of the particle distribution. For the clouds that are brighter than 50 G, this assumption has little effect because the errors induced in the Rayleigh component of the scattering profile are small compared to the ice component. The non-linear least-squares fit is performed using the MPFIT routine in the IDL language that is publically available in the SOLARSOFT data analysis package [Freeland and Bently, 2000]. This routine is an implementation of the Levenberg-Marquardt method [Levenberg, 1944; Marquardt, 1963] commonly used in the solar radiance community [e.g. Rodgers et al. 2006].

Once the four parameters are obtained, the Rayleigh component of the scattering profile is calculated from Equation 2 and removed to yield A_{ice}. As mentioned previously, we refer to A_{PMC} as the albedo observed at $\Theta = 90°$ and the phase function is then unity at that angle. There is nothing in the above procedure that enforces this result, although the retrieved values at 90° are typically within the range 0.8 to 1.2. We determine the scaling factor to A_{PMC} which normalizes the P_{ice} to 1.0 at 90 scattering angle and adjust A_{PMC} and P_{ice} accordingly.

Figure 4 illustrates the process described above. Sample retrievals are shown for scattering profiles containing both a 10G and a 50G PMC from Orbit 1113. The observed albedos are shown as symbols while the retrieved Rayleigh and PMC components of the scattering profile are shown as dashed and dotted lines. The sum of these components is shown as a solid line and overlays the observations very well. Figure 4 shows how the PMC has little affect on the observations for $\Theta > 120°$ as mentioned above.

6.0 Results

The procedure outlined in Section 5 is applied to Orbits 684 and 1113. Before we examine the retrieved phase functions, we plot in Figure 5 the retrieved cloud albedos as a function of solar zenith angle. The albedos are in the range of 0 to 50 G. This range of brightness is greater than that of PMC albedos reported by a long time series of SBUV experiments [Deland et al., 2003;

2007]; however, their resolution is 150 x 150 km at cloud height, compared with that of CIPS (5 x 5 km). The comparison of PMC albedoes , binned to the coarser resolution of SBUV/2 on NOAA-17 shows an overall agreement to within ±10% [Benze et al, this issue, 2008]

Before we can discuss the retrieved phase functions, it is important to assess the reasonableness of the separation of the PMC and Rayleigh components of the observed albedos. In order to do this, we examine calculated values of the nadir viewing Rayleigh albedo. We compare values of this quantity obtained from analytic retrievals of C and σ in locations where there are no PMC to a similar calculation with C and σ obtained from the non-linear least-squares fit at locations where a PMC is present. The presence or non-presence of a PMC is indicated by RATALL as described above. The comparison is made for locations in bins of 1° of solar zenith angle. We use the nadir viewing Rayleigh brightness because it allows us to compare results from scattering profiles obtained at different locations and different observation angles. If at one solar zenith angle, we get similar results for the Rayleigh albedo obtained from different techniques and with and without the presence of a PMC, then the technique is valid. The only assumption is that ozone does not vary appreciably between locations at the same solar zenith angle (or essentially latitude). If this assumption is not valid, then we will obtain a poor comparison between the two sets of results. The nadir viewing Rayleigh albedo is calculated with Equation 2 by setting $\phi = 0°$ ($\mu_V = 1$).

This comparison is shown in two ways in Figure 5. Figure 5a is for Orbit 684 and Figure 5b is for Orbit 1113. The calculated nadir viewing Rayleigh albedos are shown as dark dots for locations with no PMC present and light dots for locations where a PMC is present. The overlap of the two populations as a function of solar zenith angle shows that the agreement is very good. To get a better understanding of the differences, at each solar zenith angle we calculate the mean nadir albedo for each population and take the ratio. This ratio is plotted in Figure 5 as a function of solar zenith angle using as asterisks. A solid line shows a constant value of 1.0 which would

indicate perfect agreement. The surrounding dotted lines are ±2.5% of 1.0. Figures 5a and 5b show that the mean differences between the retrieved albedos for the two populations are within 2.5% for most solar zenith angles. The differences exceed this value only for very high solar zenith angles where the Rayleigh albedo is weak. To give a feel for the reasonableness of agreement within 2.5%, we note that a 10 G PMC superimposed upon a 100 G Rayleigh background will have about a 25% random uncertainty in its albedo. The exact uncertainty varies with solar zenith angle but this is a good average. As shown in Figure 5a and especially in Figure 5b, there are many clouds with albedos brighter than 10G and so have smaller uncertainties.

Figure 6 plots all the phase functions obtained between 60° and 90° solar zenith angle for PMC with A_{PMC} within 1 G of 10, 20, 30, and 40 G. The panels also list the mean value of R_m, 53 ± 15 nm, 59 ± 10 nm, 56 ± 18 nm, and 55 ± 7 nm respectively obtained for each of the these sets of PMCs. Figure 6 also plots the theoretical curves for the T-matrix phase functions for the assumptions listed in Section 5 for the mean value of R_m as well as R_m plus and minus one standard deviation. The shape of the retrieved phase functions is generally very similar to the T-matrix functions. While numerical representations of the phase functions are required by the algorithms, there is nothing in the process that forces the results to look similar to the representative functions.

Figure 6 shows that there is much more variability in the phase functions, and therefore the particle sizes, for the dimmer clouds. As the cloud albedo increases, the phase functions become more consistent. Some of the variability in the 10 G phase functions is due to the larger uncertainties due to the lower brightness, but as stated above the average uncertainty for individual albedo observations of this brightness is about 25% and so a significant portion of the noise must also be geophysical. It should be remembered that while the observed brightness of a PMC is typically dominated by the size of the particles and the observing geometry, all geometry factors including those depending on particle size are removed in our retrieved A_{PMC} and so this

318 value is primarily dependent upon ice number density. Figure 6 suggests that when ice densities
319 are at their lowest, perhaps either early or late in the their lifetime, PMC show the largest
320 variability in particle sizes, but when PMC are at their peak in ice densities, the particle sizes
321 tend to stabilize.

322 It should be emphasized that these values of particle mode radius, R_m, are valid for the
323 assumptions of the particle distribution listed in Section 5. The phase functions could be
324 interpreted with other assumptions and different values of R_m would be obtained. We could have
325 also used a different set of assumptions in the retrieval stage, this again would yield a different
326 value of R but there would be little impact on the phase functions themselves. For example, we
327 performed the retrieval using phase functions for spherical particles with the same Gaussian
328 distribution width used for the oblate particles. The retrieved R_m values were different, but the
329 retrieved phase functions were not different at any scattering angle to better than 2%. The
330 conclusion is that CIPS can do an excellent job of retrieving the phase function of the observed
331 PMC ice, but the interpretation of those phase functions to yield particle sizes is dependent upon
332 assumptions made.

333 **7.0 Summary and Conclusions**

334 We have developed an algorithm that uses the CIPS data to retrieve values of PMC albedo and
335 phase functions. The CIPS absolute albedo measurements have been shown to be consistent with
336 those measured by the well calibrated SBUV instruments [Benze et al. 2008, this issue]. The
337 results for particle phase functions and albedo, under the assumptions discussed in Sections 5
338 and 6, are very reasonable and compare favorably with models [Rapp and Thomas, 2006] and
339 other measurements [Gumbel et al., 2001]. The spatial resolution of the CIPS instrument, 5 km,
340 allows for the detection and derivation of the properties, of thousands of clouds each orbit
341 [McClintock et al. 2008, this issue]. The results for a complete season will provide an
342 unprecedented look at PMC properties including albedo, phase functions, and ice content as a

function of time and location.

The other AIM remote sensing instrument, SOFIE [Gordley et al., 2008] views the same region of space as CIPS once each orbit. SOFIE results [Hervig et al. 2008, this issue] provide particle properties at this location. Future studies using the combination of SOFIE and CIPS data will take advantage of this unique observational scenario for cross validation and further definition of cloud properties for microphysical studies.

Acknowledgements

AIM was developed as part of NASA's Small Explorer series of missions. We gratefully acknowledge the support of the Explorer's program and the efforts of the entire AIM development, science, and operations teams.

References

Bailey, S. M., A. W. Merkel, G. E. Thomas, and J. N. Carstens, Observations of Polar Mesospheric Clouds from the SNOE satellite, *J. Geophy. Res*., 110, D13, D13203, 10.1029/20004JD005422, 2005.

Bailey, S. M., A. W. Merkel, G. E. Thomas, and D. W. Rusch, Interhemispheric differences in polar mesospheric cloud morphology observed by the Student Nitric Oxide Explorer, *J. Atmos. Sol. Terr. Phys.*, 69. 12. 1407-1418, 2007.

Bates, D. R., Rayleigh Scattering by Air, *Planetary and Space Science*, Vol. 32, pp. 785-790 1984.

Benze, S. C. E. Randal, M. T. DeLand, G. E. Thomas, D. W. Rusch, S. C. Bailey, J. M. Russell III, W. E. McClintock, A. W. Merkel, C. Jeppesen, 2008, Comparison of Aeronomy of Ice in the Mesosphere to the Solar Backscatter Ultraviolet Instrument, *J. Atmos. Sol. Terr. Phys.,* this issue.

Berger, U., and F.-J. Lübken, Weather in mesospheric ice layers, *Geophys. Res. Lett*., 33, 2006.

Chapman, S., The Absorption and Dissociative or Ionizing Effect of Monochromatic Radiation in the Atmosphere on a Rotating Earth, *Proc. Roy. Soc.*, **43**, 483-501, 1931.

370 DeLand, M. T., E. P. Shettle, G. E. Thomas, and J. J. Olivero, Solar backscattered ultraviolet
371 (SBUV) observations of polar mesospheric clouds over two solar cycles, J.Geophys. Res.
372 108(D8), 8445, doi:10.1029/2002JD002398, 2003.
373 DeLand M. T., E. P. Shettle, G. E. Thomas, J. J. Olivero, Latitude-dependent long-term
374 variations in polar mesospheric clouds from SBUV version 3 PMC data, J. Geophys. Res.,
375 112, D10315, doi:10.1029/2006JD007857, 2007.
376 Eremenko, M. N., S. V. Petelina, A. Y. Zasetsky, B. Karlsson, C. P. Rinsland, E. J. Llewellyn,
377 and J. J. Sloan, Shape and composition of PMC particles derived from satellite remote
378 sensing measurements, *Geophys. Res. Lett.,* 32, L16S06, doi:10.1029/2005GL023013, 2005.
379 Fitzmaurice, J. A., Simplification of the Chapman Function for Atmospheric Attenuation,
380 *Appl. Opt*., **3**, 640, 1964.
381 Freeland, S. L. and R. D. Bently, Solarsoft, *Encyl. Astron. Astrophys*., Inst. Of Phys. Bristol, U.
382 K., 2922-2925, 2000.
383 Gordley, L.L., M. Hervig, C. Fish,…, The Solar Occultation For Ice Experiment, J. Atmos. and
384 Solar-Terrestrial Phys., in review, 2007.
385 Gumbel, J., J. Stegman, D. P. Murtagh, and G. Witt, Scattering phase functions and particle sizes
386 in noctilucent clouds, Geophys. Res. Lett., 28(8), 1415-1418, 2001
387 Hedin, A. E., MSIS-90 Thermospheric model, *J. Geophys. Res*., **96**, 1159-1172, 1991.
388 Hervig, M.E., L.L. Gordley, M. Stevens, J.M. Russell, and S. Bailey, Interpretation of SOFIE
389 PMC measurements: Cloud identification and derivation of mass density, particle shape, and
390 particle size, J. Atmos. Solar-Terr. Phys., in review, 2008.
391 Karlsson, B., H. Kornich, and J. Gumbel (2007), Evidence for interhemispheric stratosphere-
392 mesosphere coupling derived from noctilucent cloud properties, *Geophys. Res. Lett*., 34,
393 L16806, doi:10.1029/2007GL030282.
394 Levenberg, K. A., A method for the solution of certain non-linear problems in least squares, Q.
395 Appl. Math, 2, 164-168, 1944.
396 Leslie, R. J., 1885, Sky Glows, *Nature (London)*, *34*, 264.
397 Marquardt, D. W., An algorithm for least-squares estimation of nonlinear parameters, *J. Soc.*
398 *Indust. Appl. Math*, 11, 2, 1963.

399 McClintock, D. W. Rusch, G. E. Thomas, A. W. Merkel, S. M. Bailey, J. M. Russell III, 2008,
400 The Cloud Imaging and Particle Size Experiment on the Aeronomy of Ice in the Mesosphere
401 Mission; Instrument concept, design, calibration, and on-orbit performance, J. Atmos. Sol.
402 Terr. Phys., this issue.
403 McPeters, R., D. The Behavior of Ozone Near the Stratopause From Two Years of BUV
404 Observations, J. Geophys. Res., 85, 4545-4550, 1980.
405 Merkel, A. W., C. A. Barth, S. M. Bailey, Altitude determination of ultraviolet measurements
406 made by the Student Nitric Oxide Explorer, *J. Geophys. Res*., 106, A12, 30,283, 2001.
407 Mishchenko, M. I., and L. D. Travis, Capabilities and limitations of a current FORTRAN
408 implementation of the T-matrix method for randomly oriented, rotationally symmetric
409 scatterers, J. Quant. Spectrosc. Radiat. Transfer, 60, 309 – 324, 1998.
410 Rapp, M., and G. E. Thomas, Modeling the microphysics of mesospheric ice particles:
411 assessment of current capabilities and basic sensitivities, J. Atmos. Sol. Terr. Phys.. Vol. 68,
412 715-744, 2006.
413 Rapp, M., G. E. Thomas, and G. Baumgarten, Spectral properties of mesospheric ice clouds:
414 Evidence for nonspherical particles, J. Geophys. Res., VOL. 112, D03211,
415 doi:10.1029/2006JD007322, 2007.
416 Rusch, D. W., S. M. Bailey, G. E. Thomas, and A. W. Merkel, Seasonal-latitudinal Variations of
417 PMC Particle Size from SME Measurements for the Northern 1983 Season and SNOE
418 Measurements for the Northern 2000 and Southern 2000/2001 Seasons, *J. Atmos. Sol. Terr.*
419 *Phys.*, 70, doi: 10.1016/j.jastp.2007.10.006, 2008.
420 Rusch, D. W., G. E. Thomas1, W. McClintock, A. W. Merkel, S. M. Bailey, J. M. Russell III, C.
421 E. Randall, C. Jeppesen, and M. Callan, The Cloud Imaging and Particle Size Experiment on
422 the Aeronomy of Ice in the Mesosphere Mission: Cloud Morphology for the Northern 2007
423 season, *J. Atmos. Solar-Terr. Phys*., in review, 2008.
424 Russell III, James M., Scott M. Bailey, Mihály Horányi, Larry L. Gordley, David W. Rusch,
425 Mark E. Hervig, Gary E. Thomas, Cora E. Randall, David E. Siskind, Michael H. Stevens,
426 Michael E. Summers, Michael I. Taylor, Christoph R. Englert, Patrick J. Espy, William E.
427 McClintock and Aimee W. Merkel, 2008, Aeronomy of Ice in the Mesosphere (AIM):
428 Overview and early science results, *J. Atmos. Solar-Terr. Phys*., in review.

429 Rodgers, E. M., S. M. Bailey, H. P. Warren, T. N. Woods, and F. G. Eparvier, Solar flare soft X-
430 ray irradiance from observations by TIMED SEE, JGR, 111, A10S13,
431 doi:10.1029/2005JA011505, 2006.
432 Shettle, E. P., Thomas, G. E., Olivero, J. J., Evans, W. F. J., Debrestian, D. J., Chardon, L.,
433 2002b. Three-satellite comparison of polar mesospheric clouds: Evidence for long-term
434 change. J. Geophys. Res. 107(D12), 10.1029/2001JD000668, 2002.
435 Thomas, G. E., Solar Mesosphere Explorer measurements of polar mesospheric clouds
436 (noctilucent clouds*), J. Atmos. Terr. Phys*., 46, 819, 1984.
437 Thomas, G. E., Are noctilucent clouds harbingers of global change in the middle atmosphere?,
438 *Adv. Space Res., 32*, 9, 1737-1746, 2003.
439 Thomas, G.E., and C.P. McKay, On the mean particle size and water content of polar
440 mesospheric clouds, *Planet. Space Sci., 33*, No. 10, 1209-1224, 1985.
441 Thomas, G. E., Olivero, J. J., Deland, M., Shettle, E. P., 2003. Comment on Are noctilucent
442 clouds truly a "miner's canary" for global change? EOS 84 (36), 2003.
443 von Savigny, C., S. V. Petelina, B. Karlsson, E. J. Llewellyn, D. A. Degenstein, N. D. Lloyd, and
444 J. P. Burrows (2005), Vertical variation of NLC particle sizes retrieved from Odin/OSIRIS
445 limb scattering observations, Geophys. Res. Lett., 32, L07806, doi:10.1029/2004GL021982.
446 von Zahn, U. 2003. Are noctilucent clouds truly a "miner's canary" for global change? EOS 84
447 (28).
448
449
450

Appendix: Derivation of the C – Sigma Algorithm

Our goal is to provide an analytic description of the Rayleigh brightness with a minimum of free parameters. An overview of the physics of the problem and a relevant figure can be found in Merkel et al. [2001]. At 265 nm, there is only one scattering of sunlight from atmospheric molecules. Photons are removed along the path through absorption by O_3. We neglect attenuation by Rayleigh scattering which is known to yield only a 1% effect [McPeters, 1980].

For one infinitesimal altitude level, z, the contribution to the observed intensity is

$$dI = dz \frac{n_{air}(z)\beta P_{Ray}(\Theta)F}{\mu_V} \exp\left[-\left(\frac{1}{\mu_V}+\frac{1}{\mu_z}\right)\left(\tau_\beta+\tau_\alpha\right)\right]. \qquad \text{(A1)}$$

τ_β, and τ_α are the vertical optical depths due to Rayleigh scattering and pure absorption by ozone,

$$\begin{aligned} \tau_\beta(z) &= \beta\int_z^\infty n_{air}(z)dz = N(z)\beta \\ \tau_\alpha(z) &= \alpha\int_z^\infty n_{O3}(z)dz = X(z)\alpha \end{aligned} \quad . \qquad \text{(A2)}$$

N(z) and X(z) are the air and ozone column densities respectively.

The observed intensity and therefore the Earth albedo is obtained by the following integral,

$$A = \frac{I}{F} = \int_0^\infty d\tau_\beta \frac{P_{Ray}(\Theta)}{\mu_V} \exp\left[-\left(\frac{1}{\mu_V}+\frac{1}{\mu_z}\right)\left(\tau_\beta+\tau_\alpha\right)\right] . \qquad \text{(A3)}$$

Letting C be the ozone column density at reference altitude z_0, the altitude dependent column density of ozone, X, can be written as

$$X = C\left(\frac{N}{N_0}\right)^{1/\sigma} \qquad \text{(A4)}$$

where N_0 is the air column density above z_0,

$$N(z) = N_0 \exp\left[-\int_z^\infty dz' \frac{1}{H_{air}(z)} \right] \quad \text{(A5)}$$

where H_{air} is the altitude-dependent scale height of air. We define σ as the ratio of the ozone to air scale height,

$$\sigma = \frac{H_{ozone}}{H_{air}} \quad . \quad \text{(A6)}$$

We assume that σ is constant with altitude. This does not require that either scale height in Equation A6 is constant, only the ration of the two scale heights.

Equation A4 is rewritten in terms of optical depth to show

$$\tau_\alpha{}^\sigma = \tau_{\alpha 0}{}^\sigma \frac{\tau_\beta}{\tau_{\beta 0}} \quad . \quad \text{(A7)}$$

Ignoring attenuation by Rayleigh scattering as mentioned above, we then rewrite Equation A3 as

$$A = P_{Ray}(\Theta) \int_0^\infty \frac{d\tau_\beta}{\mu_V} \exp\left[-\left(\frac{1}{\mu_V} + \frac{1}{\mu_z} \right) (\tau_\alpha) \right] \quad . \quad \text{(A8)}$$

Letting k represent the term in parenthesis,

$$A = \frac{P_{Ray}(\Theta)}{\mu_V} \int_0^\infty d\tau_\beta e^{-k\tau_\alpha} \quad , \quad \text{(A9)}$$

which can be rewritten and solved with a Laplace transform,

$$\int d\tau_\alpha \frac{d\tau_\beta}{d\tau_\alpha} e^{-k\tau_\alpha} = k \int d\tau_\alpha \tau_\beta(\tau_\alpha) e^{-k\tau_\alpha} \quad \text{(A10)}$$

which is valid as long as $\tau_\beta(\tau_\alpha)=0$ which is true in this case (all optical depths are zero at the top

484 of the atmosphere). Thus Equation A9 is rewritten as

485 $$A = \frac{P_{Ray}(\Theta)}{\mu_V} \int_0^\infty d\tau_\alpha \frac{\tau_{\beta_0}}{{\tau_{\alpha_0}}^\sigma} {\tau_\alpha}^\sigma e^{-k\tau_\alpha} \quad . \quad \text{(A11)}$$

486 Through some manipulation and use of the gamma function Equation A11 becomes

487 $$A = \frac{P_{Ray}(\Theta)}{\mu_V} \frac{\tau_{\beta_0}}{{\tau_{\alpha_0}}^\sigma} \left(\frac{1}{k}\right)^\sigma \Gamma(\sigma+1) \quad . \quad \text{(A12)}$$

488 Using the definition of k, Equation A12 yields

489 $$A_{Ray} = \frac{P_{Ray}(\Theta)\Gamma(\sigma+1)\beta N(z_0)}{\mu_V \left(\frac{1}{\mu_V} + \frac{1}{\mu_Z}\right)^\sigma \alpha^\sigma C(z_0)^\sigma} \quad \text{(A13)}$$

490 which is Equation 2.

Figure Captions

Figure 1. Scattering and solar zenith angles for each observation of orbit 424 on May 24, 2007 (dots). The 7 observations for 13 individual locations are shown as asterisks connected by solid lines. The 7 observations of albedo form the scattering profile for those locations. Latitudes are shown at the top of the figure.

Figure 2. Representative scattering profiles at 4 solar zenith angles from orbit 424 on May 24, 2007 (top row). Circles are for observations at scattering angles less than 90° while squares are observations at scattering angles greater than 90°. The inferred values of C and σ for each scattering profile are listed. In the bottom row, derived values of Y are plotted against the geometry factors X for each of the above scattering profiles. Fitted lines are also shown.

Figure 3. Distribution of RATALL values for Orbits 424, 684, and 1113.

Figure 4. Sample retrievals for scattering profiles containing a 10G (left panel) and a 50G (right panel) PMC from Orbit 1113. Points are observed albedo. Circles are for observations at scattering angles less than 90° and squares are observations at scattering angles greater than 90°. Dotted lines with pluses are the retrieved cloud albedo. Dashed lines with pluses are retrieved Rayleigh albedo. The sum of the retrieved cloud and Rayleigh albedos are shown as solid lines.

Figure 5a. Ratio of the nadir viewing Rayleigh albedo as calculated from the retrieved Rayleigh parameters for observations with a PMC present to the same value for observations where no PMC is present. The mean value of this ratio for observations with solar zenith angles within 1° of select solar zenith angles are shown as asterisks. Vertical lines reflect the mean plus and minus one standard deviation. The solid horizontal line shows a constant value of 1.0. The dotted lines are 2.5% above and below 1.0. Dark dots show the retrieved Rayleigh albedo (scaled as shown) for observations where no PMC is detected. Light dots show the retrieved albedo (scaled as shown) inferred from observations where a PMC is detected. Pluses show the retrieved cloud albedos. All values are for orbit 684.

Figure 5b. Same as Figure 5a but for Orbit 1113.

Figure 6. Retrieved phase functions for Orbit 1113 for PMC with albedos within 1G of 10, 20, 30, and 40G. Solid lines are theoretical phase functions for the shown mean radius. (See text for assumptions regarding theoretical phase functions). Dotted and dashed lines are theoretical phase functions for the shown mean radius minus and plus the shown standard deviation respectively.

Figure

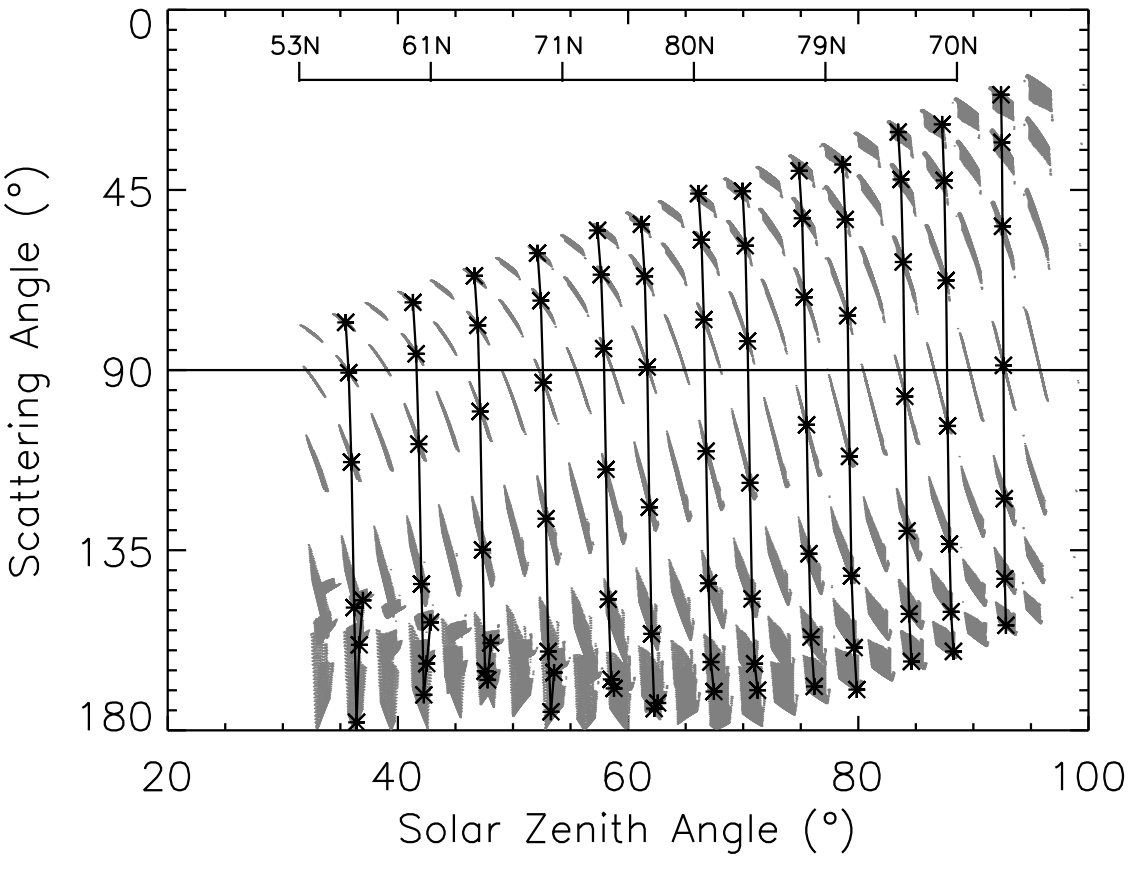
53N
61N
71N
80N
79N
70N
0
45
90
135
180
Scattering Angle (°)
20
40
60
80
100
Solar Zenith Angle (°)

Figure

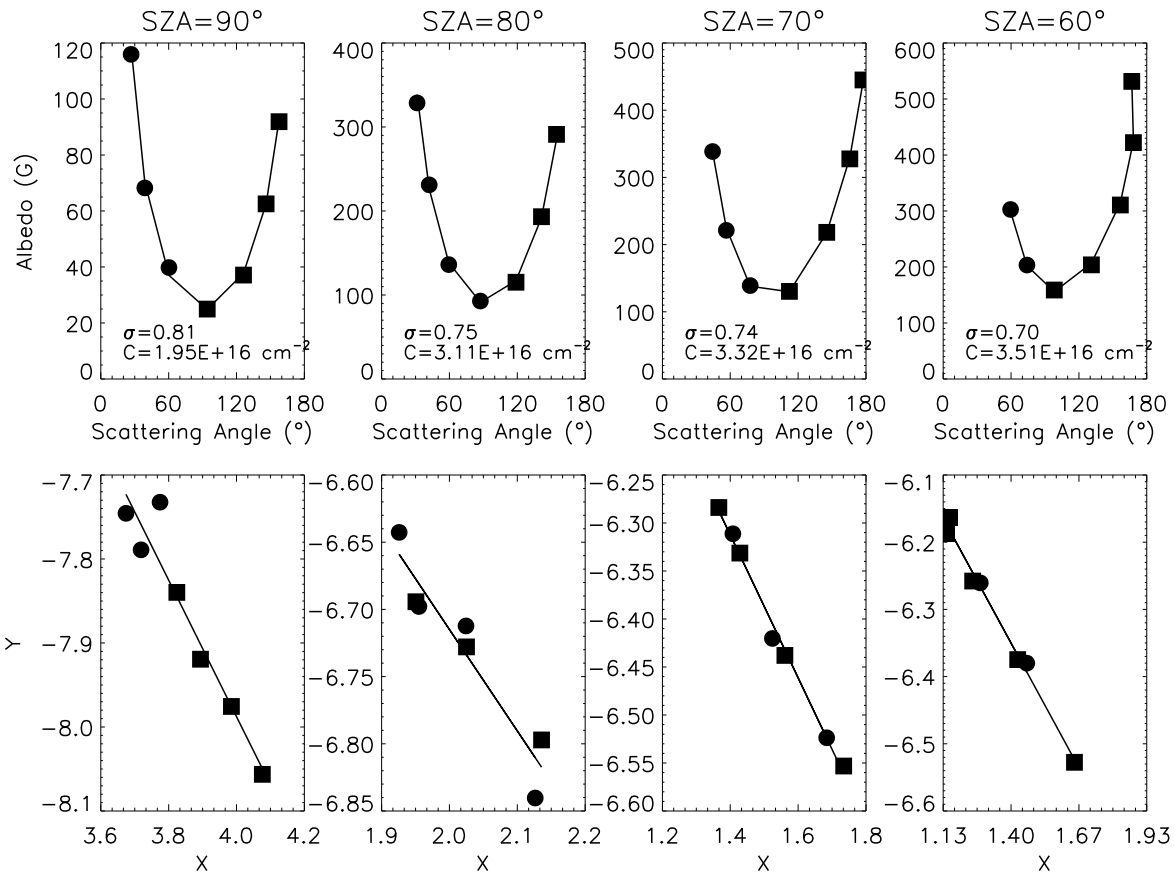
SZA=90°
SZA=80°
SZA=70°
SZA=60°
Albedo (G)
σ=0.81
C=1.95E+16 cm⁻²
σ=0.75
C=3.11E+16 cm⁻²
σ=0.74
C=3.32E+16 cm⁻²
σ=0.70
C=3.51E+16 cm⁻²
Scattering Angle (°)
Y
X

Figure

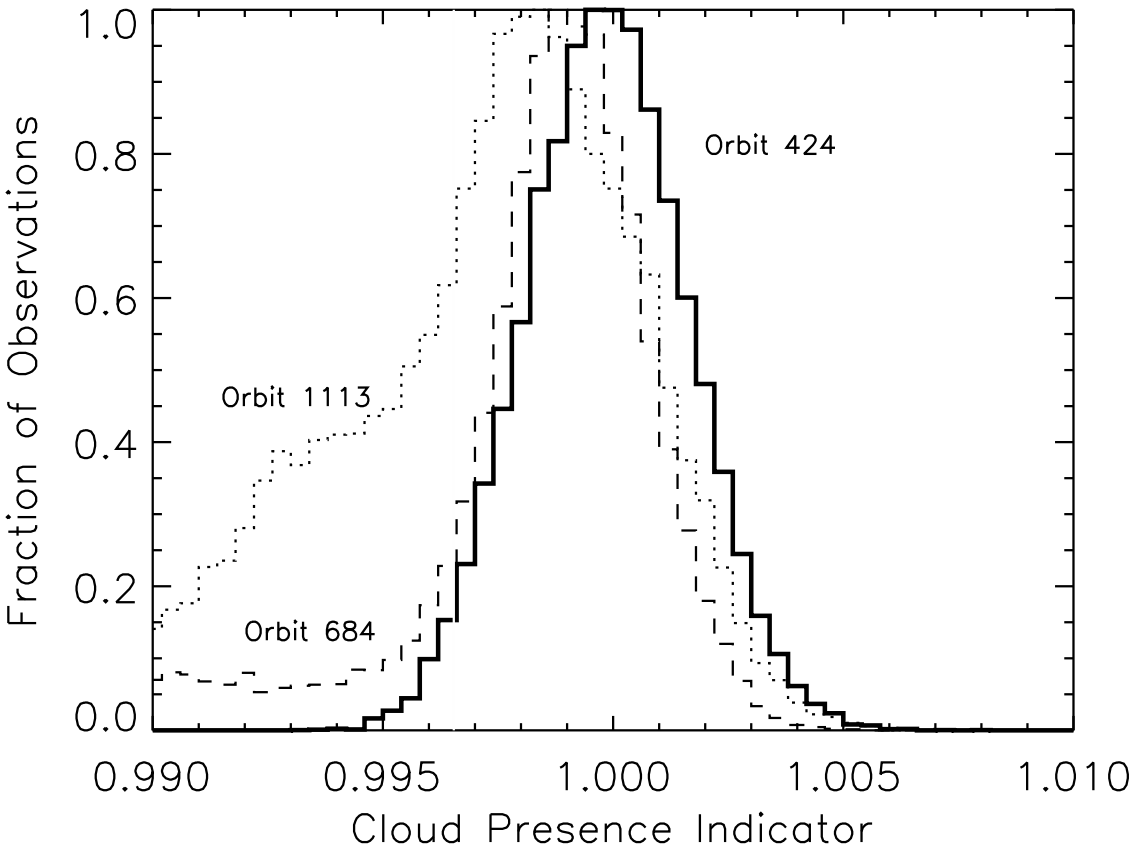
1.0
0.8
0.6
0.4
0.2
0.0
Fraction of Observations
Orbit 424
Orbit 1113
Orbit 684
0.990
0.995
1.000
1.005
1.010
Cloud Presence Indicator

Figure

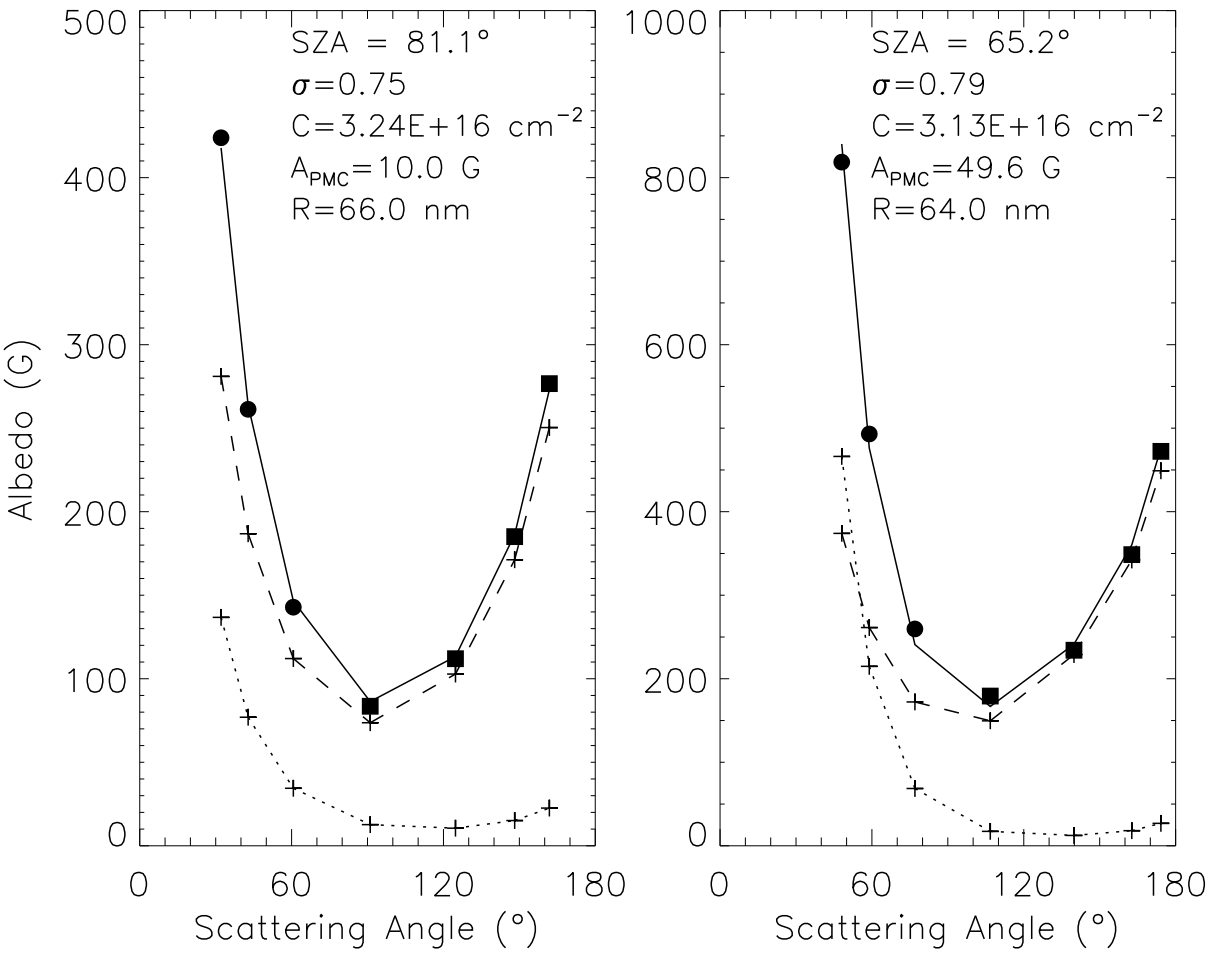
SZA = 81.1°
σ=0.75
C=3.24E+16 cm⁻²
A_PMC=10.0 G
R=66.0 nm
SZA = 65.2°
σ=0.79
C=3.13E+16 cm⁻²
A_PMC=49.6 G
R=64.0 nm
Albedo (G)
Scattering Angle (°)
Scattering Angle (°)
0
100
200
300
400
500
0
200
400
600
800
1000
0
60
120
180
0
60
120
180

Figure

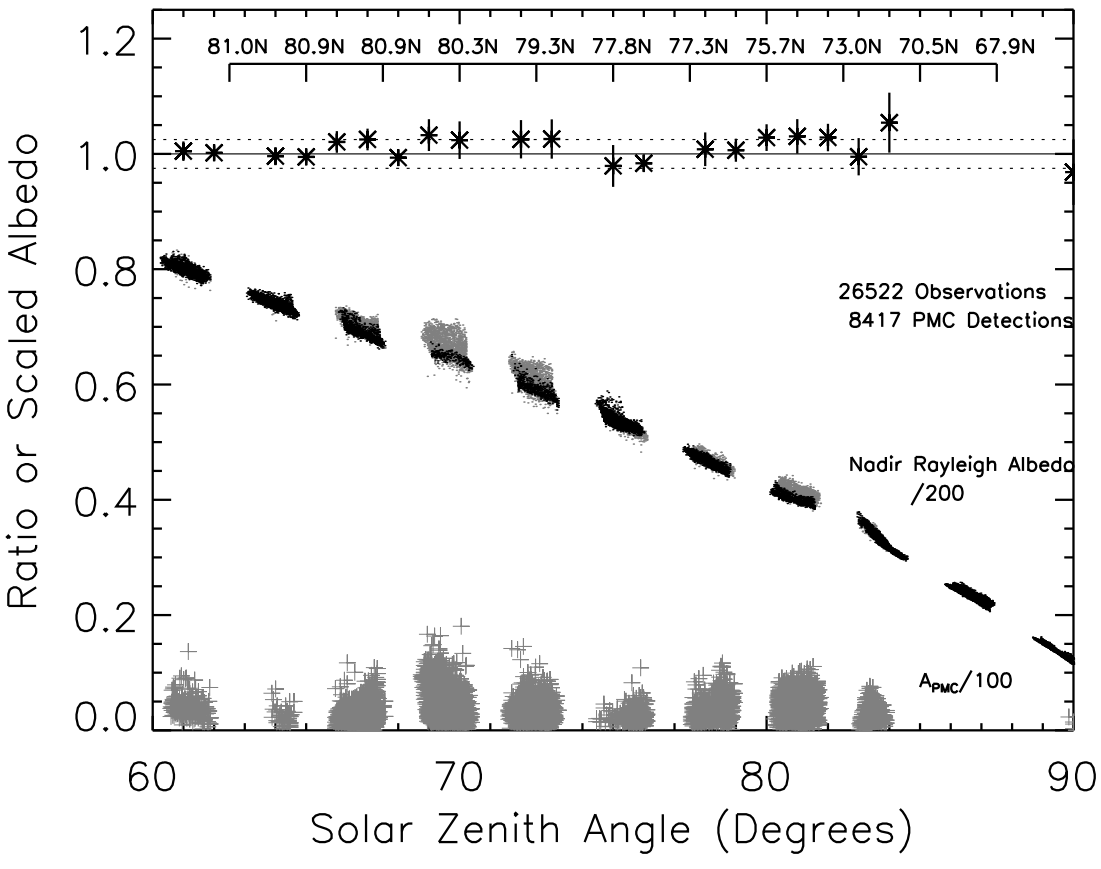
81.0N 80.9N 80.9N 80.3N 79.3N 77.8N 77.3N 75.7N 73.0N 70.5N 67.9N
26522 Observations
8417 PMC Detections
Nadir Rayleigh Albedo
/200
A_{PMC}/100
Ratio or Scaled Albedo
Solar Zenith Angle (Degrees)
0.0
0.2
0.4
0.6
0.8
1.0
1.2
60
70
80
90

Figure

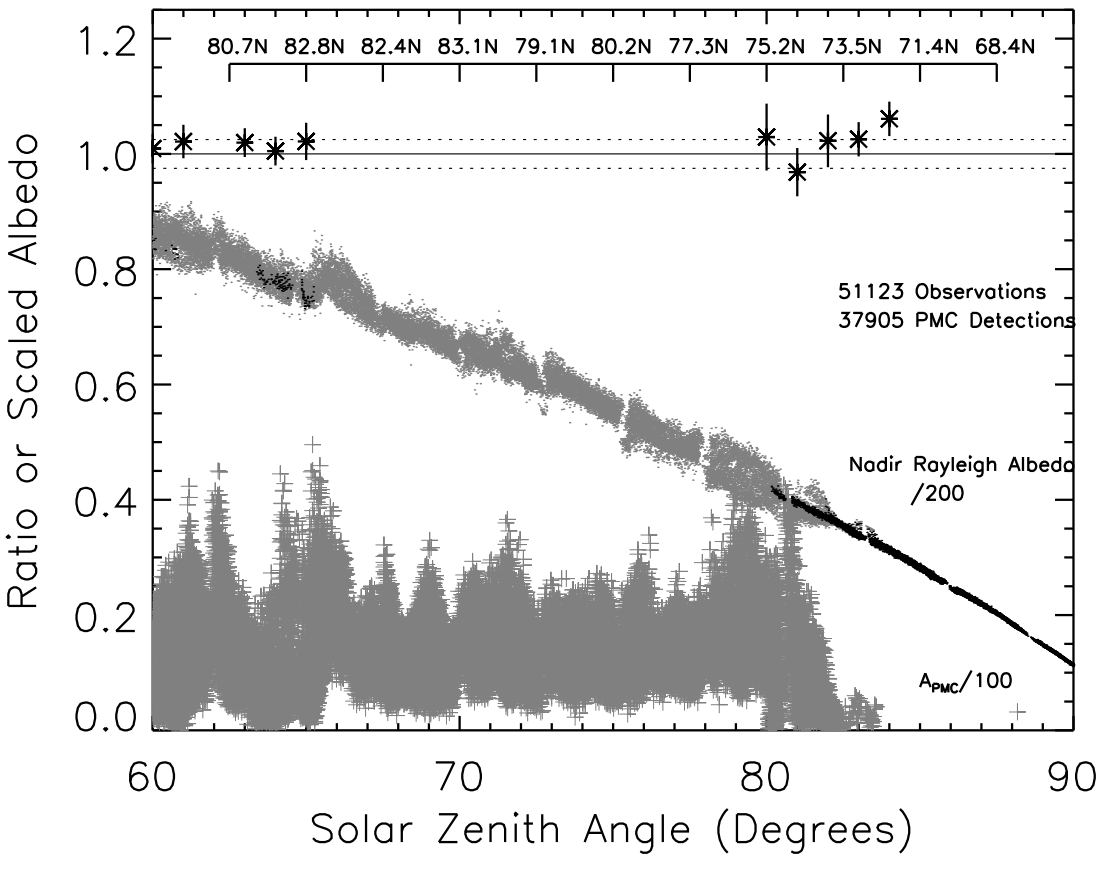
80.7N 82.8N 82.4N 83.1N 79.1N 80.2N 77.3N 75.2N 73.5N 71.4N 68.4N
51123 Observations
37905 PMC Detections
Nadir Rayleigh Albedo
/200
A_{PMC}/100
Ratio or Scaled Albedo
Solar Zenith Angle (Degrees)
0.0
0.2
0.4
0.6
0.8
1.0
1.2
60
70
80
90

Figure

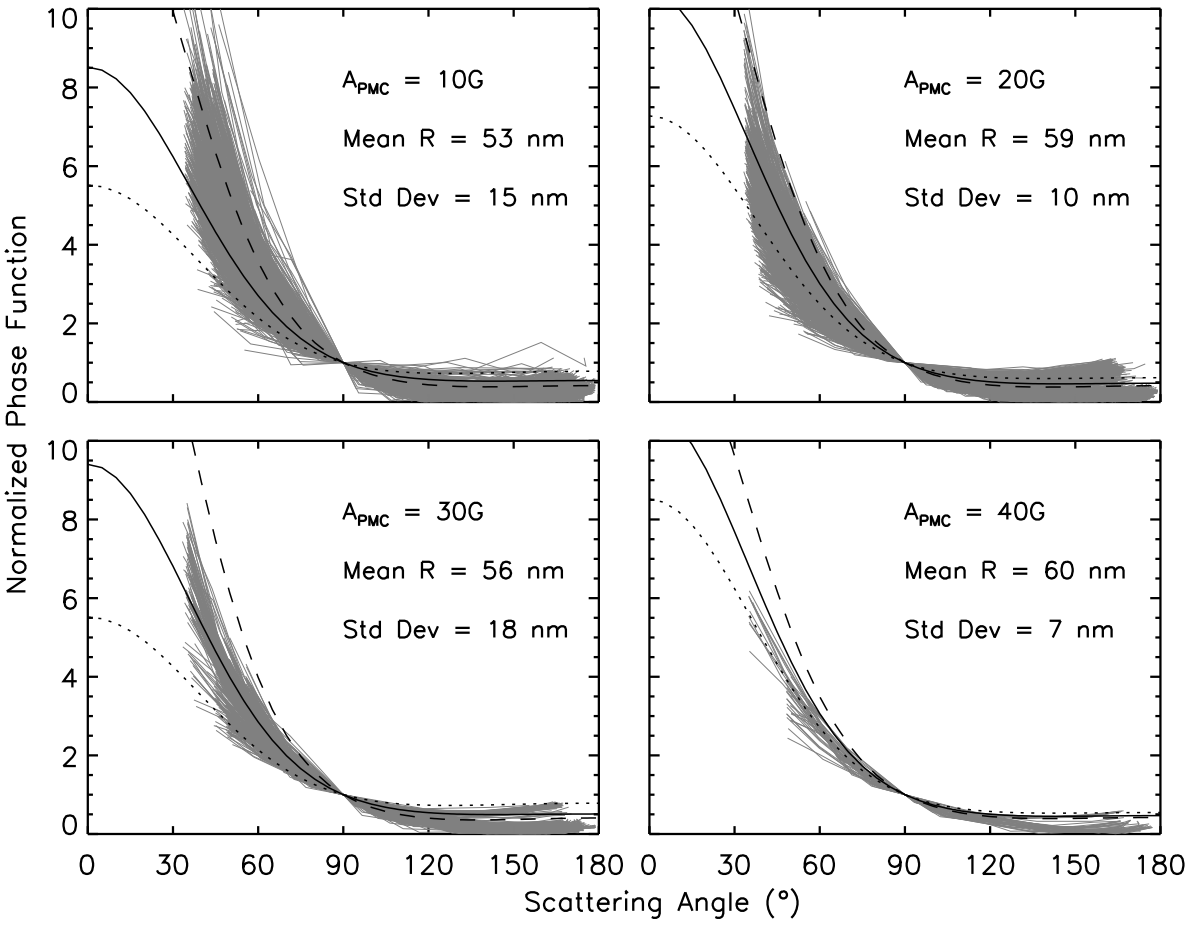
A_PMC = 10G
Mean R = 53 nm
Std Dev = 15 nm
A_PMC = 20G
Mean R = 59 nm
Std Dev = 10 nm
A_PMC = 30G
Mean R = 56 nm
Std Dev = 18 nm
A_PMC = 40G
Mean R = 60 nm
Std Dev = 7 nm
Normalized Phase Function
Scattering Angle (°)
0
2
4
6
8
10
0
30
60
90
120
150
180